

TrofyBot: A Transformable Rolling and Flying Robot with High Energy Efficiency

Mingwei Lai^{1,2}, Yuqian Ye^{1,3}, Hanyu Wu^{1,4}, Chice Xuan¹, Ruibin Zhang^{1,2}, Qiuyu Ren^{1,2},
Chao Xu^{1,2}, Fei Gao^{1,2}, and Yanjun Cao^{1,2}

Abstract—Terrestrial and aerial bimodal vehicles have gained significant interest due to their energy efficiency and versatile maneuverability across different domains. However, most existing passive-wheeled bimodal vehicles rely on attitude regulation to generate forward thrust, which inevitably results in energy waste on producing lifting force. In this work, we propose a novel passive-wheeled bimodal vehicle called TrofyBot that can rapidly change the thrust direction with a single servo motor and a transformable parallelogram linkage mechanism (TPLM). Cooperating with a bidirectional force generation module (BFGM) for motors to produce bidirectional thrust, the robot achieves flexible mobility as a differential driven rover on the ground. This design achieves 95.37% energy saving efficiency in terrestrial locomotion, allowing the robot continuously move on the ground for more than two hours in current setup. Furthermore, the design obviates the need for attitude regulation and therefore provides a stable sensor field of view (FoV). We model the bimodal dynamics for the system, analyze its differential flatness property, and design a controller based on hybrid model predictive control for trajectory tracking. A prototype is built and extensive experiments are conducted to verify the design and the proposed controller, which achieves high energy efficiency and seamless transition between modes.

I. INTRODUCTION

In recent years, terrestrial and aerial bimodal vehicles (TABVs) have drawn increasing attention. Equipped with flying and driving mechanisms, they have both advantages of unmanned aerial and ground vehicles, including excellent crossing-domain mobility and long endurance [1]–[13]. TABVs use passive or active wheels for ground movements. Passive-wheeled TABVs rely on horizontal component of the thrust to move on the ground. Since the thrust is always in the direction of vertical upwards relative to the body frame, they must adjust the pitch angle around their equilibrium attitude to accelerate or decelerate [9]–[15]. The power used for the vertical component of the thrust is meaningless. Therefore, the energy-saving advantage of TABVs has not been fully utilized, as much energy is wasted on generating lifting force which is actually unnecessary in terrestrial mode.

Apart from energy waste, attitude regulation also causes the sensors to rotate with the body, which can lead to fluctuating field of view (FoV) for sensors like cameras or

This work was supported by National Nature Science Foundation of China under Grant No. 62103368. (Corresponding authors: Yanjun Cao.)

¹ Huzhou Institute of Zhejiang University, Huzhou, 313000, China.

² State Key Laboratory of Industrial Control Technology, Institute of Cyber-Systems and Control, Zhejiang University, Hangzhou, 310027, China.

³ Stanford University, Stanford, CA 94305, USA

⁴ ETH Zürich, 8092 Zürich, Switzerland.

E-mails: {mw lai, yanjunhi}@zju.edu.cn

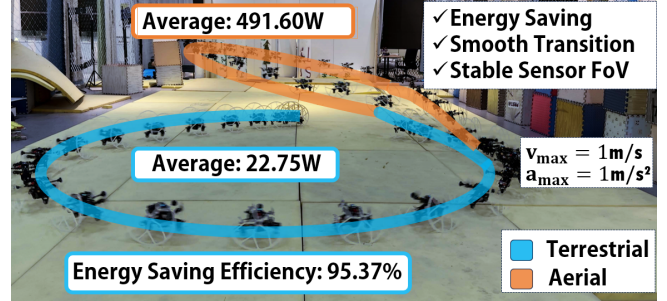


Fig. 1: Illustration of a hybrid trajectory tracking with TrofyBot. Experiment shows that motion in terrestrial mode requires only 4.63% of the energy used in aerial mode at the same motion speed, 95.37% of the energy saved.

2-D radars [9], [11], [14], [15]. It is detrimental to obstacle avoidance and mapping tasks.

To address the aforementioned issues, we propose a novel passive-wheeled TABV that features a transformative capability to rapidly change the thrust direction. We named the robot as **TrofyBot**, an abbreviation of **T**ransformable **r**olling and **f**lying **r**oBot. The main novelty of our design comes from a pitch-torque balanced transformable parallelogram linkage mechanism (TPLM) combined with flexible thrust generation that utilizes bidirectional rotor control. By analyzing the kinematics and dynamics, we formulate the differential flatness property and utilize the MINCO trajectory class [16] to generate flat-output trajectories. Then we design a model-based hybrid nonlinear model predictive control (HNMPCC) controller to achieve accurate trajectory tracking performance in both terrestrial mode and aerial mode, as well as seamless transition between two modes.

By incorporating a single extra servo motor based on previous work [15], TrofyBot achieves much higher energy efficiency. In terrestrial mode, it can keep the thrust always aligned with the moving direction, maximizing energy utilization while providing high acceleration and strong turning torque. Experiments show that motion in terrestrial mode requires only 4.63% of the energy used in aerial mode at the same motion speed, as illustrated in Fig.1. At the same time, accurate tracking performance is achieved from great maneuverability and the HNMPCC controller. Moreover, without the need of attitude regulation for ground motion as noted [15], TrofyBot can maintain a stable body attitude that is conducive to perception, such as providing a favorable FoV for the onboard camera sensors. Last but not least, TrofyBot achieves smooth mode transitions by relying solely on the control of its servo motor, which takes less than 100ms to

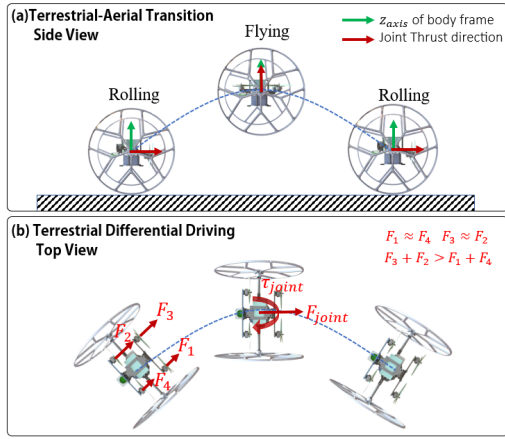


Fig. 2: The mode transition and ground turning movements.

rotate through an angle of $\pi/2$, as shown in Fig. 2. To sum up, the main contributions of this work are as followings:

- 1) A novel passive-wheeled TABV features a pitch-torque balanced transformable parallelogram linkage mechanism combined with bidirectional rotor control, which achieves high energy efficiency in terrestrial mode.
- 2) A bimodal dynamic model of the proposed TABV, including the corresponding differential flatness which contributes to simplifying trajectory planning.
- 3) A HNMPC controller that achieves accurate trajectory tracking performance in both terrestrial and aerial mode, as well as seamless transition between two modes.
- 4) Extensive experiments that validate the energy efficiency and performance of the proposed controller.

II. RELATED WORK

A. TABV Mechanism Design

According to the driving mechanisms, TABVs can be primarily divided into several categories: active-wheeled, passive-wheeled and adaptive-structured. Active-wheeled based TABVs [1]–[4] install independently driven active wheels in terrestrial mode and fly as multicopters in aerial mode. As the active-wheeled systems usually include a full driving system, weight is increased and the flight time is greatly decreased. [6], [7] adopt adaptive structure to enable ground movements, but fail to achieve smooth mode transition. Passive-wheeled TABVs are usually consist of two free-rotating wheels configured besides flying platforms, which can be further subdivided into quadrotors-based and bicopters-based. Bimodal bicopters [10], [11] are equipped with two motors and two servo motors. [10] uses servo motors to directly produce heading thrust to avoid frequent attitude regulation. Quadrotor-based TABVs [5], [9], [12], [15] have passive wheels mounted onto a general quadrotor. However, the mentioned passive-wheeled TABVs all produce unnecessary lifting force on the ground.

B. Control

Robot control in aerial mode for TABVs is often similar to traditional multicopters, but control in terrestrial mode

requires precise analysis due to the nonholonomic constraints introduced by ground contact. PID-based cascaded controller is adopted in work [10], [14], [17], [18], but they oversimplify the terrestrial model for ignoring the nonlinear dynamics. Therefore, the cascaded controller is restricted to low-speed trajectory tracking. Zhang et al. [15] propose a unified nonlinear model predictive control (NMPC) method, which reveals a significant improvement compared to their previous work [14]. NMPC can directly handle dynamic constraints such as velocity limits and allow the TABVs to better track aggressive trajectory. Although NMPC often demands more computing time than no-predictive methods, previous works [9], [11], [15], [19] have shown that is acceptable even in devices with relatively low computing resources.

III. HARDWARE DESIGN

The advantages of TrofyBot come from a novel hardware design, including a pitch-torque balanced transformable parallelogram linkage mechanism (TPLM) and a bidirectional force generation module (BFGM) that can generate flexible thrust with bidirectional rotor control.

A. Design of Pitch-Torque Balanced TPLM

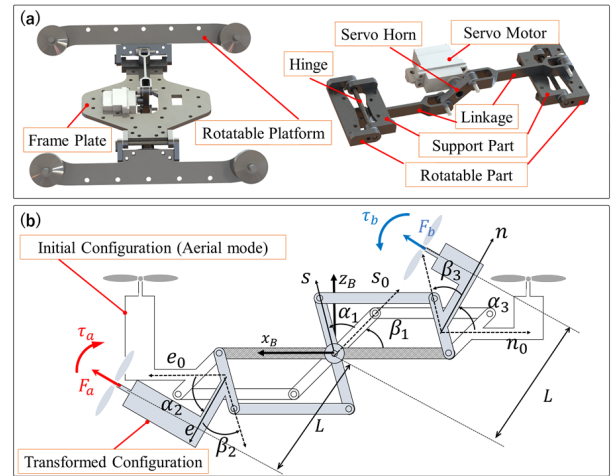


Fig. 3: (a) The hardware components of TPLM. (b) The working principle of TPLM.

TPLM can consistently adjust all four motor orientations using a single servo motor. As shown in Fig. 3a, TPLM consists of a servo motor, two linkages, two hinges, two support parts and two rotatable platforms. The servo motor and its supporting components are securely attached to the main frame plate of TrofyBot. The support parts are fixed on the frame plate. When the servo motor rotates, it utilizes the servo horn to actuate the linkage. This linkage, in turn, drives the rotatable platform mounted on the pivoting section, allowing it to rotate around the hinge and thereby adjust the direction of the thrust. In Fig. 3b, two parallelograms are formed by seven joint axes. We define (s_0, s) , (e_0, e) and (n_0, n) to represent the initial and real-time position of the servo horn, the left rotatable part and the right rotatable platform, respectively, and define α_1 , α_2 and α_3 to represent their rotating angle. When the servo horn is at s_0 , the two

TABLE I: Model and Weight of Components

Component	Model	Weight(g)
Battery	iFlight Fullsend LR 4000mAh 6s	433.5
Onboard Computer	NVIDIA Jetson Xavier NX	72
Seovo Motor	GDW DS290IG	40
Brushless Motors	T-Motor F60Pro KV1750	130
Propellers	GEMFAN 51477 5-inch	16.5
Passive Wheels	Monomer Casting Nylon	200
Flight Controller	Kakute H7 Mini	8
ESC	Holybro Tekko32 45A	7

rotatable parts are at e_0 and n_0 , respectively. e_0 and n_0 are aligned with the support parts. When installing the servo horn, we make sure that when α_2 is $\pi/4$, s is perpendicular to e_0 . Then we will get $\beta_1 = \pi/4$. β_2 and β_3 are set to $\pi/4$ and are established upon completion. Leveraging the parallelograms we can get

$$\alpha_1 + \beta_1 = \alpha_2 + \beta_2 = \alpha_3 + \beta_3 \Rightarrow \alpha_1 = \alpha_2 = \alpha_3 \quad (1)$$

Therefore, the motor orientations are always consistent.

Furthermore, TPLM simplifies pitch axis attitude regulation. We define the forces on both sides as F_a and F_b and torques on both side as τ_a and τ_b . They have equal lever arm length L . That means

$$L \times F_a = L \times F_b \Rightarrow \tau_a = \tau_b. \quad (2)$$

The torques on both sides are always balanced. When F_a is close to F_b , the pitch axis attitude remains stable unless significantly affected by external torques.

B. Implementation of BFGM

BFGM generates bidirectional thrust which facilities the ground motion maneuverability greatly. The hardware details are shown in Fig. 4 where the BFGM is indicated. The model and weight of the components are listed in Table. I.

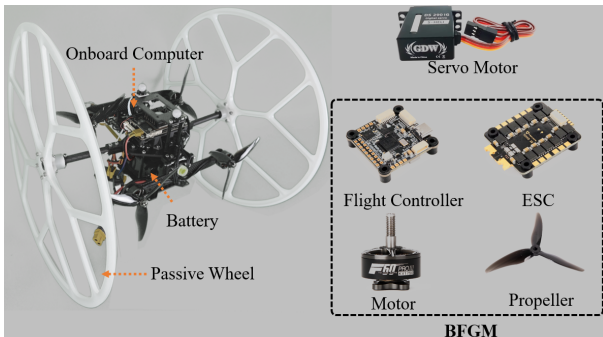


Fig. 4: The hardware details of TrofyBot. BFGM is indicated by a black dashed rectangle.

BFGM consists of a flight controller, a electronic speed controller (ESC), four motors and four propellers. We adopt bidirectional mode of the ESC, and modify the ArduPilot firmware for the flight controller so that we can control

each motor in a closed-loop manner. The motor can rotate bidirectionally, and it can switch between the two directions in less than 200ms even in high speed. Note that we still use standard propellers but we perform precise calibration between rotary speed and thrust force, the results show a higher forward thrust coefficient $c_{t,f}$ than reverse $c_{t,r}$. With BFGM, TrofyBot can perform fast acceleration and deceleration maneuvers as well as execute aggressive turns.

IV. BIMODAL DYNAMICS AND CONTROL

In this section, we analysis the kinematics and dynamics of TrofyBot firstly. Then we formulate the differential flatness property and design a model-based hybrid nonlinear model predictive control (HNMPC) controller.

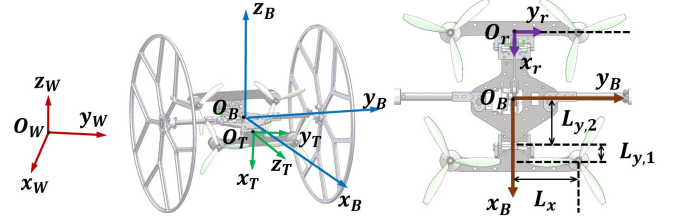


Fig. 5: The coordinate frames of the dynamics model of TrofyBot.

A. Dynamics analysis of TrofyBot

Four coordinate frames used are defined in Fig. 5, including world frame (\mathcal{F}_W) with z_W pointing opposite to the gravity vector, body frame (\mathcal{F}_B) with z_B perpendicular to the frame plate and y_B aligned with the wheel axle, the hinge frame (\mathcal{F}_T) with its origin at the hinge center, z_T perpendicular to the front rotatable platform and y_T parallel to y_B , and the rotatable platform frame (\mathcal{F}_r) with x_r coincides with x_B , y_r parallel to y_B and y_r passing through the center of the propeller. We introduce three Euler angles $[\phi, \theta, \psi]^T$ to describe the rotation of \mathcal{F}_B relative to \mathcal{F}_W , and introduce $L_x, L_{y,1}, L_{y,2}$ to calculate variable inertia matrix and allocation matrix.

We describe the dynamics model of TrofyBot in a separate manner, as a general quadrotor model in aerial mode and as a differential-driven model in terrestrial mode. We define λ as the angle by which \mathcal{F}_T rotates around y_B relative to \mathcal{F}_B . Note that λ remains zero in the air.

The aerial translational dynamics are given by

$$\dot{\mathbf{p}}_W = \mathbf{v}_W, \quad (3)$$

$$\dot{\mathbf{v}}_W = -g\mathbf{z}_W + \frac{T}{m}\mathbf{z}_B + \frac{\mathbf{F}_e}{m}, \quad (4)$$

where \mathbf{p}_W and \mathbf{v}_W are the position and velocity in \mathcal{F}_W , respectively. (4) includes three factors that contribute to the linear acceleration: the gravitational acceleration g pointing downward, the total rotors thrust T and the external disturbance force vector \mathbf{F}_e . m is the mass of TrofyBot.

The aerial rotational dynamics are given by

$$\dot{\mathbf{q}} = \frac{1}{2}\mathbf{q} \circ \begin{bmatrix} 0 \\ \mathbf{w}_B \end{bmatrix}, \quad (5)$$

$$\dot{\mathbf{w}}_B = \mathbf{J}^{-1}(\boldsymbol{\tau}_B + \boldsymbol{\tau}_e - \mathbf{w}_B \times \mathbf{J}\mathbf{w}_B), \quad (6)$$

where $\mathbf{q} = [q_w, q_x, q_y, q_z]^T$ is the unit quaternion attitude vector, $\mathbf{w}_B = [w_{B,x}, w_{B,y}, w_{B,z}]^T$ is the angular velocity in \mathcal{F}_B and \circ is the Hamilton product. The matrix \mathbf{J} is the moment of inertia tensor, $\boldsymbol{\tau}_B$ is the control moment vector and $\boldsymbol{\tau}_e$ is the external disturbance moment vector. \times is the cross product.

In terrestrial mode, we assume that the ground is flat and the wheels have no lateral slip. Then the terrestrial translational dynamics are given by

$$\dot{\mathbf{p}}_W = \begin{bmatrix} v_l \cos \psi \\ v_l \sin \psi \\ 0 \end{bmatrix}, \quad (7)$$

$$\dot{v}_l = \frac{T \sin(\theta + \lambda) + F_e}{m}, \quad (8)$$

where v_l is a scalar representing the longitudinal velocity and F_e representing the longitudinal external disturbance force. The lateral velocity is constrained to zero, so the velocity is always aligned with T and is totally longitudinal.

The terrestrial rotational dynamics are given by (6) and

$$\begin{bmatrix} \dot{\phi} \\ \dot{\theta} \\ \dot{\psi} \end{bmatrix} = \begin{bmatrix} 0 \\ w_{B,y} \\ w_{B,z} \sec \theta \end{bmatrix}. \quad (9)$$

Due to the absence of singularity issues on the ground, we directly use Euler angles to describe the rotational dynamics.

Unlike general quadrotors, the inertia tensor matrix and allocation matrix would vary with λ . We define M as the allocation Matrix and $\mathbf{t} = [t_1, t_2, t_3, t_4]^T$ as the rotor thrust vector. M satisfies

$$\begin{bmatrix} T \\ \boldsymbol{\tau}_B \end{bmatrix} = M \mathbf{t} \quad (10)$$

We only consider the principal moments of inertia, namely J_{xx} , J_{yy} and J_{zz} . Then \mathbf{J} is given by

$$\begin{cases} J_{xx} = 2[J_{r,xx} \cos^2 \lambda + J_{r,zz} \sin^2 \lambda + m_r(L_{y,1} \sin \lambda)^2] \\ \quad + J_{s,xx}, \\ J_{yy} = 2m_r[(L_{y,1} + L_{y,2} \cos \lambda)^2 + (L_{y,2} \sin \lambda)^2] \\ \quad + 2J_{r,yy} + J_{s,yy}, \\ J_{zz} = J_{s,zz} + 2(J_{r,zz} \cos^2 \lambda + J_{r,xx} \sin^2 \lambda) \\ \quad + 2m_r(L_{y,2} + L_{y,1} \cos \lambda)^2, \end{cases} \quad (11)$$

where \mathbf{J}_r is the inertia tensor matrix of the rotatable platform with two motors in \mathcal{F}_r . m_r is the mass of the platform with two motors. \mathbf{J}_s is the inertia tensor matrix of the remaining part, excluding the two rotatable parts. M is given by

$$M = \begin{bmatrix} 1 & 0 & 0 & 0 \\ 0 & L_x \cos \lambda & 0 & \frac{c_m}{c_t} \sin \lambda \\ 0 & 0 & L_{y,1} + L_{y,2} \cos \lambda & 0 \\ 0 & -L_x \sin \lambda & 0 & \frac{c_m}{c_t} \cos \lambda \end{bmatrix} \cdot V, \quad (12)$$

where c_m and c_t are the rotor torque and thrust coefficient respectively. Note that c_t is subdivided into $c_{t,f}$ in forward direction and $c_{t,r}$ in reverse direction. The factor Matrix V in (12) is

$$V = \begin{bmatrix} v_1 \\ v_2 \\ v_3 \\ v_4 \end{bmatrix} = \begin{bmatrix} 1 & 1 & 1 & 1 \\ -1 & 1 & 1 & -1 \\ -1 & 1 & -1 & 1 \\ -1 & -1 & 1 & 1 \end{bmatrix}. \quad (13)$$

To sum up, the state vector of the hybrid system is $\mathbf{X} = [\mathbf{p}_I^T, \mathbf{v}_I^T, v_l, \theta, \psi, \mathbf{q}^T, \mathbf{w}_B^T]^T$ and the input vector is $\mathbf{U} = [\mathbf{t}^T, \lambda]^T = [t_1, t_2, t_3, t_4, \lambda]^T$. $\mathbf{X}_t = [\mathbf{p}_I^T, v_l, \theta, \psi, \mathbf{w}_B^T]^T$ and $\mathbf{X}_a = [\mathbf{p}_I^T, \mathbf{v}_I^T, \mathbf{q}^T, \mathbf{w}_B^T]^T$ are the state vectors in terrestrial and aerial mode, respectively. We use $f(\mathbf{X}, \mathbf{U})$ to represent the system dynamics.

B. Differential Flatness

Both the terrestrial and aerial dynamics of TrofyBot are differentially flat, which is leveraged to simplify trajectory optimization. As the differential flatness in aerial mode as a general quadrotor has been well studied in previous work, we refer readers to [20]–[23] for details, where $\boldsymbol{\sigma}_a = [\mathbf{p}_{W,x}, \mathbf{p}_{W,y}, \mathbf{p}_{W,z}, \psi]^T$ is typically chosen as the flat output. This section will demonstrate the differential flatness in terrestrial mode.

The system uses $[t_1, t_2, t_3, t_4, \lambda]^T$ to control four degrees of freedom $[\mathbf{p}_{W,x}, \mathbf{p}_{W,y}, \theta, \psi]^T$ when on the ground. But ψ is constrained by the ground contact, which is given as

$$\psi = \arctan 2(\eta \dot{\mathbf{p}}_{W,y}, \eta \dot{\mathbf{p}}_{W,x}), \quad (14)$$

where η indicates the motion direction of TrofyBot (forward when $\eta = 1$ and backward when $\eta = -1$).

In addition, to maximize energy efficiency, we keep \mathbf{z}_T parallel to the ground, namely

$$\lambda = \frac{\pi}{2} - \theta. \quad (15)$$

When in terrestrial locotion, $\lambda \approx \frac{\pi}{2}$, so $\tau_{B,x} \approx \frac{c_m}{c_t} \sin \lambda \cdot \mathbf{v}_4$ according to (12). We expect $\tau_{B,x} = 0$, which means

$$t_1 + t_2 - t_3 - t_4 = 0. \quad (16)$$

Considering (14), (15), (16), essentially we get three independent inputs to control three degrees of freedom $[\mathbf{p}_{W,x}, \mathbf{p}_{W,y}, \theta]^T$. Therefore, we define the flat output in terrestrial locomotion as

$$\boldsymbol{\sigma}_t = [\mathbf{p}_{W,x}, \mathbf{p}_{W,y}, \theta]^T. \quad (17)$$

To demonstrate terrestrial differential flatness, we need to derive every state in \mathbf{X}_t from $\boldsymbol{\sigma}_t$ and its derivatives.

We can directly get \mathbf{p}_W and θ from $\boldsymbol{\sigma}_t$ and get angular velocity from θ and ψ

$$w_{B,y} = \dot{\theta}, \dot{w}_{B,y} = \ddot{\theta}, \quad (18)$$

$$w_{B,z} = \dot{\psi} \cos \theta, \dot{w}_{B,z} = \ddot{\psi} \cos \theta - \dot{\psi} \sin \theta \cdot \dot{\theta}. \quad (19)$$

v_l is given by

$$v_l = \eta \sqrt{(\dot{\mathbf{p}}_{W,x})^2 + (\dot{\mathbf{p}}_{W,y})^2}. \quad (20)$$

By substituting (20) into (8) and ignoring F_e , the total thrust

is given by

$$T = m\dot{v}_l = m \frac{\ddot{p}_{W,x}\dot{p}_{W,x} + \ddot{p}_{W,y}\dot{p}_{W,y}}{\sqrt{(\dot{p}_{W,x})^2 + (\dot{p}_{W,y})^2}}. \quad (21)$$

Then by combining (6), (11), (15), (16), (18) and (19) we can get τ_B . Finally we obtain t with T and τ_B substituted into the inverse form of (10).

Till now, all state and input variables are derived from the flat output. Therefore, we can summarize that the terrestrial dynamics of TrofyBot is differentially flat.

C. HNMPC

We design a HNMPC controller by employing a discrete switching variable to accurately distinguish the subsystem dynamics. The control system is shown in Fig. 6. We get a flat-output trajectory from MINCO [16], then derive the whole reference trajectory utilizing the differential flatness. The controller automatically decides the switching variable l according to the reference p_z .

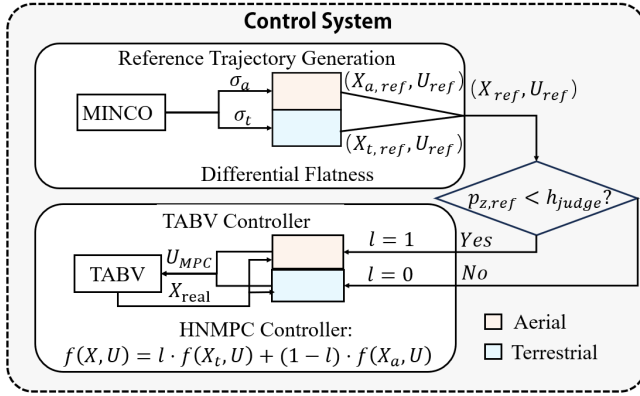


Fig. 6: The control system of TrofyBot.

The HNMPC finds the best control commands by solving an optimal control problem (OCP) in a receding horizon manner. It aims at minimizing a cost function measuring the errors between the predicted states and the reference trajectory in the time horizon $[t, t + K \cdot dt]$. The time horizon is discretized into K equal intervals with a fixed time step dt .

We describe the whole system dynamics as

$$f(\mathbf{X}, \mathbf{U}) = l_k f(\mathbf{X}_t, \mathbf{U}) + (1 - l_k) f(\mathbf{X}_a, \mathbf{U}). \quad (22)$$

Then the HNMPC problem is formulated as

$$\begin{aligned} \mathbf{u}_{MPC} = \min_{\mathbf{u}} \quad & \sum_{i=k}^{k+N-1} [l_k \cdot \tilde{\mathbf{x}}_{t,i}^T \mathbf{W}_{x,t} \tilde{\mathbf{x}}_{t,i} \\ & + (1 - l_k) \cdot \tilde{\mathbf{x}}_{a,i}^T \mathbf{W}_{x,a} \tilde{\mathbf{x}}_{a,i} + \tilde{\mathbf{u}}_i^T \mathbf{W}_u \tilde{\mathbf{u}}_i] \\ & + l_k \cdot \tilde{\mathbf{x}}_{t,N}^T \mathbf{W}_{x,t} \tilde{\mathbf{x}}_{t,N} + (1 - l_k) \tilde{\mathbf{x}}_{a,N}^T \mathbf{W}_{x,a} \tilde{\mathbf{x}}_{a,N}, \\ \text{s.t.} \quad & \mathbf{x}_{i+1} = f(\mathbf{x}_i, \mathbf{u}_i), \mathbf{u}_{\min} < \mathbf{u}_i < \mathbf{u}_{\max}, \end{aligned} \quad (23)$$

where l_k is the discrete variable, it is given by

$$l_k = \begin{cases} 1, & \text{if reference } p_{W,z,k} < h_{judge}, \\ 0, & \text{if reference } p_{W,z,k} > h_{judge}, \end{cases} \quad (24)$$

TABLE II: Table of Parameters. $D()$ represents $diag([\])$ as diagonal matrix.

Physical	Value	HNMPCC	Value
m, m_r [kg]	1.25, 0.2	N, dt	40, 0.05
\mathbf{J}_s [$g \cdot m^2$]	$D(7.3, 4, 7.7)$	W_{v_l}	100
\mathbf{J}_r [$g \cdot m^2$]	$D(0.14, 0.08, 0.12)$	W_λ	1
c_m [$N \cdot m \cdot s^2$]	$2.56e^{-10}$	\mathbf{W}_p	$D(5000, 5000, 3000)$
$c_{t,f}$ [$N \cdot s^2$]	$1.6e^{-8}$	\mathbf{W}_v	$D(10, 10, 10)$
$c_{t,r}$ [$N \cdot s^2$]	$7.79e^{-9}$	\mathbf{W}_{w_B}	$D(100, 100, 10)$
$L_{y,1}, L_{y,2}$ [m]	0.02, 0.04	W_θ, W_ψ	100, 100
L_x, h_{judge} [m]	0.05, 0.12	\mathbf{W}_t	$D(10, 10, 10, 10)$

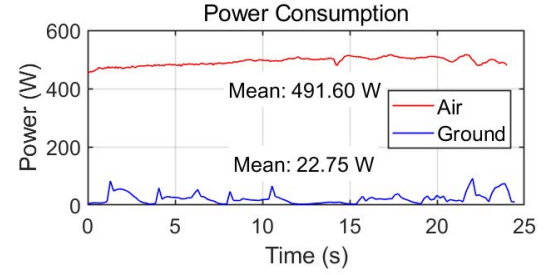


Fig. 7: Power consumption for equivalent trajectories in two modes. The motion in terrestrial mode requires only 4.63% of the energy used in aerial mode at the similar motion speed.

where h_{judge} is greater than the radius of the wheel. k is the current time step, $\tilde{\mathbf{x}}_{t,i} = \mathbf{x}_{t,ref,i} - \mathbf{x}_{t,i}$, $\tilde{\mathbf{x}}_{a,i} = \mathbf{x}_{a,ref,i} - \mathbf{x}_{a,i}$ and $\tilde{\mathbf{u}}_i = \mathbf{u}_{ref,i} - \mathbf{u}_i$ are the terrestrial states, aerial states and inputs error, respectively. $\tilde{\mathbf{x}}_{t,N}$ and $\tilde{\mathbf{x}}_{a,N}$ are the end states error. $\mathbf{W}_{t,x}$, $\mathbf{W}_{a,x}$ and \mathbf{W}_u are the terrestrial states, aerial states and inputs weight matrix written as

$$\begin{aligned} \mathbf{W}_{t,x} &= diag([\mathbf{W}_p, W_{v_l}, W_\theta, W_\psi, \mathbf{W}_w]), \\ \mathbf{W}_{a,x} &= diag([\mathbf{W}_p, \mathbf{W}_v, \mathbf{W}_q, \mathbf{W}_w]), \\ \mathbf{W}_u &= diag([\mathbf{W}_t, W_\lambda]). \end{aligned} \quad (25)$$

V. EXPERIMENTS

We build a prototype as shown in Fig.4. The physical parameters and the NMPC parameters are listed in Table. II. We obtain the 6D localization from a NOKOV capture system. The NMPC problem is solved by ACADO [24] with qpOASES [25] at 200 Hz. Following experiments are conducted to validate the energy efficiency and the performance of the proposed controller. It is worth noting that we fix reference θ to 0 in terrestrial mode for simplification.

A. Energy Efficiency Validation

We have the TrofyBot track two 8-shaped trajectories in aerial and terrestrial locomotion, both with maximum velocity $v_{\max} = 1m/s$, maximum acceleration $a_{\max} = 1m/s^2$ and average longitudinal velocity $v_{l,average} = 0.798m/s$. The power consumption is shown in Fig. 7. We define the average power in aerial and terrestrial mode as $P_a = 491.60W$ and $P_t = 22.75W$, respectively. Therefore, the

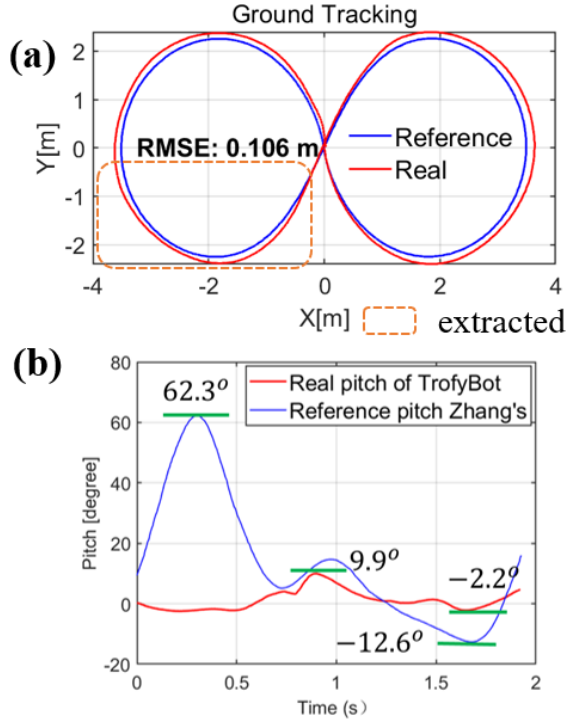


Fig. 8: (a) Reference $p_{W,xy}$ and real $p_{W,xy}$ when tracking an 8-shaped terrestrial trajectory, the orange dashed rectangular box indicates the extracted section of the trajectory. (b) Real θ of TrofyBot and reference θ of Zhang's reference trajectory from the extracted section.

energy saving efficiency is $\xi = 1 - P_t/P_a = 95.37\%$, which means the endurance in terrestrial mode is about 20 times longer than in aerial mode. The energy saving efficiency of TABV [15] is 85.7% when tracking at the same speed according to their results. The experiment demonstrates that TrofyBot achieves high energy saving efficiency for avoid generating unnecessary lifting force.

We also conduct an endurance test showing that TrofyBot can hover for 0.192 hours with power $P_h = 430.1W$. With the onboard computer running at 15W, the system can theoretically last for 2.18 hours in terrestrial mode.

B. Trajectory Tracking Control

To validate the tracking performance of the HNMPC controller, we conduct two types of tracking experiments: one involving the tracking of a terrestrial 8-shaped trajectory and another involving the tracking of a hybrid trajectory with combined terrestrial and aerial locomotion. We use root-mean-square-error(RMSE) as the criteria for trajectory tracking performance, which is formulated as

$$E_r = \sqrt{\frac{1}{N} \sum_{k=1}^N \|\tilde{p}^k - p_{ref}^k\|^2}, \quad (26)$$

where \tilde{p}^k and p_{ref}^k are the k -th sampled real and reference position, respectively.

The results of tracking terrestrial 8-shaped trajectory with $v_{max} = 3m/s$ and $a_{max} = 2.5m/s^2$ are shown in Fig. 8a.

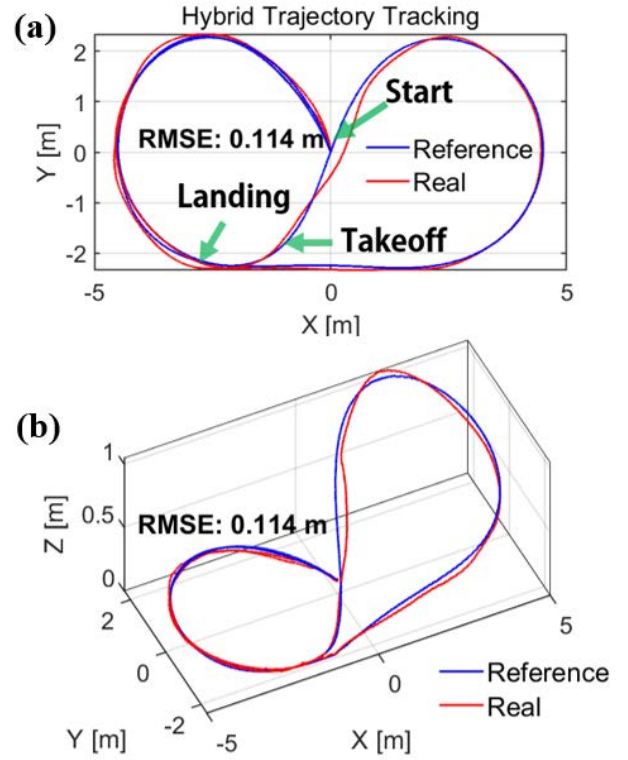


Fig. 9: Reference $p_{W,xyz}$ and real $p_{W,xyz}$ when tracking an 8-shaped hybrid trajectory, top view (a) and perspective view (b). The start position, takeoff position and land position are indicated in by green arrows in (a).

The controller maintains accurate trajectory tracking with $E_r = 0.106m$. Furthermore, we extract a segment of the trajectory as indicated by the orange dashed rectangular box. From the extracted segment, we get real θ of TrofyBot in the tracking test and reference θ based on the differential flatness property from Zhang et al. [15]. It is shown in Fig. 8b that the real θ of TrofyBot fluctuates between -2.2° and 9.9° , while Zhang's reference θ ranges from -12.6° to 62.3° . It demonstrates that TrofyBot can provide a stable sensor FoV with minimal body motion during high-speed ground movements, while TABVs requiring attitude regulation on the ground experience greater sensor FoV variations.

The results of tracking hybrid trajectory with $v_{max} = 2m/s$ and $a_{max} = 2m/s^2$ are shown in Fig. 9. The start position, takeoff position and landing position are indicated in 9a. Note that the TrofyBot, after landing, returns to the start position along the terrestrial part of the 8-shaped trajectory. The controller exhibits good hybrid tracking performance with $E_r = 0.114m$. The result validates that TrofyBot achieves smooth transition with HNMPC.

VI. CONCLUSION

In this work, we design a novel quadrotor-based TABV with two passive wheels called TrofyBot. We analyze its dynamic model and differential flatness, and propose a HNMPC controller. We conduct extensive real-world experiments, demonstrating its high energy efficiency and verifying the performance of the controller.

REFERENCES

- [1] S. Mintchev and D. Floreano, "A multi-modal hovering and terrestrial robot with adaptive morphology," in *Proceedings of the 2nd International Symposium on Aerial Robotics*, 2018.
- [2] Q. Tan, X. Zhang, H. Liu, S. Jiao, M. Zhou, and J. Li, "Multimodal dynamics analysis and control for amphibious fly-drive vehicle," *IEEE/ASME Transactions on Mechatronics*, vol. 26, no. 2, pp. 621–632, 2021.
- [3] A. Kalantari, T. Touma, L. Kim, R. Jitosho, K. Strickland, B. T. Lopez, and A.-A. Agha-Mohammadi, "Drivocopter: A concept hybrid aerial/ground vehicle for long-endurance mobility," in *2020 IEEE aerospace conference*. IEEE, 2020, pp. 1–10.
- [4] M. Cao, X. Xu, S. Yuan, K. Cao, K. Liu, and L. Xie, "Doublebee: A hybrid aerial-ground robot with two active wheels," in *2023 IEEE/RSJ International Conference on Intelligent Robots and Systems (IROS)*, 2023, pp. 6962–6969.
- [5] M. Yamada, M. Nakao, Y. Hada, and N. Sawasaki, "Development and field test of novel two-wheeled uav for bridge inspections," in *2017 International Conference on Unmanned Aircraft Systems (ICUAS)*. IEEE, 2017, pp. 1014–1021.
- [6] N. B. David and D. Zarrouk, "Design and analysis of festar, a hybrid flying and climbing sprawl tuned robot," *IEEE Robotics and Automation Letters*, vol. 6, no. 4, pp. 6188–6195, 2021.
- [7] S. Morton and N. Papanikolopoulos, "A small hybrid ground-air vehicle concept," in *2017 IEEE/RSJ International Conference on Intelligent Robots and Systems (IROS)*, 2017, pp. 5149–5154.
- [8] E. Tal and S. Karaman, "Accurate tracking of aggressive quadrotor trajectories using incremental nonlinear dynamic inversion and differential flatness," *IEEE Transactions on Control Systems Technology*, vol. 29, no. 3, pp. 1203–1218, 2021.
- [9] N. Pan, J. Jiang, R. Zhang, C. Xu, and F. Gao, "Skywalker: A compact and agile air-ground omnidirectional vehicle," *IEEE Robotics and Automation Letters*, vol. 8, no. 5, pp. 2534–2541, 2023.
- [10] J. Yang, Y. Zhu, L. Zhang, Y. Dong, and Y. Ding, "Sytab: A class of smooth-transition hybrid terrestrial/aerial bicopters," *IEEE Robotics and Automation Letters*, vol. 7, no. 4, pp. 9199–9206, 2022.
- [11] J. Lin, R. Zhang, N. Pan, C. Xu, and F. Gao, "Skater: A novel bi-modal bi-copter robot for adaptive locomotion in air and diverse terrain," *IEEE Robotics and Automation Letters*, vol. 9, no. 7, pp. 6392–6399, 2024.
- [12] A. Kalantari and M. Spenko, "Design and experimental validation of hytaq, a hybrid terrestrial and aerial quadrotor," in *2013 IEEE International Conference on Robotics and Automation*, 2013, pp. 4445–4450.
- [13] S. Latscha, M. Kofron, A. Stroffolino, L. Davis, G. Merritt, M. Piccoli, and M. Yim, "Design of a hybrid exploration robot for air and land deployment (h.e.r.a.l.d) for urban search and rescue applications," in *2014 IEEE/RSJ International Conference on Intelligent Robots and Systems*, 2014, pp. 1868–1873.
- [14] R. Zhang, Y. Wu, L. Zhang, C. Xu, and F. Gao, "Autonomous and adaptive navigation for terrestrial-aerial bimodal vehicles," *IEEE Robotics and Automation Letters*, vol. 7, no. 2, pp. 3008–3015, 2022.
- [15] R. Zhang, J. Lin, Y. Wu, Y. Gao, C. Wang, C. Xu, Y. Cao, and F. Gao, "Model-based planning and control for terrestrial-aerial bimodal vehicles with passive wheels," in *2023 IEEE/RSJ International Conference on Intelligent Robots and Systems (IROS)*, 2023, pp. 1070–1077.
- [16] Z. Wang, X. Zhou, C. Xu, and F. Gao, "Geometrically constrained trajectory optimization for multicopters," *IEEE Transactions on Robotics*, vol. 38, no. 5, pp. 3259–3278, 2022.
- [17] D. D. Fan, R. Thakker, T. Bartlett, M. B. Miled, L. Kim, E. Theodorou, and A.-a. Agha-mohammadi, "Autonomous hybrid ground/aerial mobility in unknown environments," in *2019 IEEE/RSJ International Conference on Intelligent Robots and Systems (IROS)*. IEEE, 2019, pp. 3070–3077.
- [18] J. Colmenares-Vázquez, P. Castillo, N. Marchand, and D. Huerta-García, "Nonlinear control for ground-air trajectory tracking by a hybrid vehicle: theory and experiments," *IFAC-PapersOnLine*, vol. 52, no. 8, pp. 19–24, 2019.
- [19] S. Sun, A. Romero, P. Foehn, E. Kaufmann, and D. Scaramuzza, "A comparative study of nonlinear mpc and differential-flatness-based control for quadrotor agile flight," *IEEE Transactions on Robotics*, vol. 38, no. 6, pp. 3357–3373, 2022.
- [20] D. Mellinger and V. Kumar, "Minimum snap trajectory generation and control for quadrotors," in *2011 IEEE international conference on robotics and automation*. IEEE, 2011, pp. 2520–2525.
- [21] M. Faessler, A. Franchi, and D. Scaramuzza, "Differential flatness of quadrotor dynamics subject to rotor drag for accurate tracking of high-speed trajectories," *IEEE Robotics and Automation Letters*, vol. 3, no. 2, pp. 620–626, 2017.
- [22] M. Watterson and V. Kumar, "Control of quadrotors using the hopf fibration on so (3)," in *Robotics Research: The 18th International Symposium ISRR*. Springer, 2019, pp. 199–215.
- [23] Z. Wang, C. Xu, and F. Gao, "Robust trajectory planning for spatial-temporal multi-drone coordination in large scenes," in *2022 IEEE/RSJ International Conference on Intelligent Robots and Systems (IROS)*. IEEE, 2022, pp. 12 182–12 188.
- [24] B. Houska, H. J. Ferreau, and M. Diehl, "Acado toolkit—an open-source framework for automatic control and dynamic optimization," *Optimal control applications and methods*, vol. 32, no. 3, pp. 298–312, 2011.
- [25] H. J. Ferreau, C. Kirches, A. Potschka, H. G. Bock, and M. Diehl, "qpodes: A parametric active-set algorithm for quadratic programming," *Mathematical Programming Computation*, vol. 6, pp. 327–363, 2014.